inactive state, whereas deletion of the autoinhibitory extension results in constitutive activation (*16–18*). The fit of the four principal domains and the $NH_2$-terminal extension left one small but prominent part of the $H^+$-ATPase map unoccupied to accommodate the COOH-terminal extension. This part of the map, located above the cytoplasmic end of M10 (fig. S2D), had roughly the shape and size of a membrane-spanning helix. We therefore modeled residues 884 to 920 as a predominantly α-helical structure (cyan in Fig. 1) with kinks at $Pro^{893}$, and at $Ser^{913}$ and $Thr^{914}$ to fit the map, and linked it to M10 by a stretch of extended chain. The well-defined shape and its position in the $H^+$-ATPase hexamer (fig. S3) indicate that it must be regarded as a separate domain. In accordance with its function, it is termed the regulatory (R) domain. The R domain fit puts $Ser^{913}$/$Thr^{914}$ next to the N and P domains. This is consistent with numerous second-site revertants (*7*), which require a physical interaction of these residues with the main body of the enzyme.

We investigated the effect of the R domain on the activity of the *Neurospora* plasma membrane $H^+$-ATPase with a synthetic peptide of the 38 COOH-terminal residues. Addition of this peptide stimulated the ATPase activity by as much as a factor of 10, depending on pH (Fig. 3), whereas other peptides of similar size had no effect. This suggests that the R domain exerts its regulatory function by attaching to the N domain, restricting its mobility by tethering it to the membrane. We hypothesize that the R domain is released upon phosphorylation, leaving the N domain free to move and able to deliver ATP to the P domain. An excess of R domain peptide would have the same effect, replacing the enzyme's own R domain in the binding site and thus enabling the hinge movement of the N domain. The resulting proposed mechanism of proton pumping and enzyme regulation is shown in Fig. 4.

The $H^+$-ATPase model indicates that the R domain interacts with the next-door monomer at $Gln^{624}$ and $Arg^{625}$ in helix 5 of the P domain. The arginine is completely conserved in the hexamer-forming fungal $H^+$-ATPases, which suggests that the R domain links adjacent monomers and thus has a critical role in hexamer formation. Characteristic crystalline patches of rosette-shaped particles are common in freeze-fracture replicas of starving yeast (*20*) and *Neurospora* cells (*21*). The arrays have the same unit cell parameters and morphology as single-layer two-dimensional crystals of the *Neurospora* $H^+$-ATPase (*22*). We conclude that the $H^+$-ATPase hexamers are a storage form of the inactive enzyme. The minor domain movements observed in low-resolution maps of isolated ATPase hexamers in the presence and absence of ADP (*23*) are unlikely to reflect the well-documented large conformational changes in fully active P-type ATPases.

The striking structural similarity between the $H^+$-ATPase and the distantly related $Ca^{2+}$-ATPase implies that all other P-type ATPases—including the $Na^+$,$K^+$-ATPase, the $H^+$,$K^+$-ATPase, and the heavy metal pumps—have essentially similar structures and can be modeled on the $Ca^{2+}$-ATPase. The reason for this remarkable conservation of structural detail must be strong evolutionary pressure to maintain the functional sites of each domain in their exact spatial relationship for efficient ion pumping.

### References and Notes


1. J. V. Møller, B. Juul, M. le Maire, *Biochim. Biophys. Acta* **1286**, 1 (1996).
2. D. J. Bigelow, G. Inesi, *Biochim. Biophys. Acta* **1113**, 323 (1992).
3. E. Goormaghtigh, L. Vigneron, G. A. Scarborough, J.-M. Ruysschaert, *J. Biol. Chem.* **269**, 27409 (1994).
4. C. Toyoshima, M. Nakasako, H. Nomura, H. Ogawa, *Nature* **405**, 647 (2000).
5. P. Zhang, C. Toyoshima, K. Yonekura, N. M. Green, D. L. Stokes, *Nature* **392**, 835 (1998).
6. M. Auer, G. A. Scarborough, W. Kühlbrandt, *Nature* **392**, 840 (1998).
7. P. Morsomme, C. W. Slayman, A. Goffeau, *Biochim. Biophys. Acta* **1469**, 133 (2000).
8. J. Tittor, D. Oesterhelt, E. Bamberg, *Biophys. Chem.* **56**, 153 (1995).
9. C. Zscherp, R. Schlesinger, J. Tittor, D. Oesterhelt, J. Heberle, *Proc. Natl. Acad. Sci. U.S.A.* **96**, 5498 (1999).
10. H. Luecke, *Biochim. Biophys. Acta* **1460**, 133 (2000).
11. C. Xu, W. J. Rice, W. He, D. L. Stokes, *J. Mol. Biol.* **316**, 201 (2002).
12. M. V. Ponamarev, W. A. Cramer, *Biochemistry* **37**, 17199 (1998).
13. C. R. Lancaster, H. Michel, *Structure* **5**, 1339 (1997).
14. G. Hummer, J. C. Rasaiah, J. P. Noworyta, *Nature* **414**, 188 (2001).
15. S. Lutsenko, K. Petrukhin, M. J. Cooper, C. T. Gilliam, J. H. Kaplan, *J. Biol. Chem.* **272**, 18939 (1997).
16. F. Portillo, P. Eraso, R. Serrano, *FEBS Lett.* **287**, 71 (1991).
17. R. Serrano, F. Portillo, B. C. Monk, M. G. Palmgren, *Acta Physiol. Scand. Suppl.* **607**, 131 (1992).
18. F. Portillo, *Biochim. Biophys. Acta* **1469**, 31 (1999).
19. A. Goossens, N. De La Fuente, J. Forment, R. Serrano, F. Portillo, *Mol. Cell. Biol.* **20**, 7654 (2000).
20. O. Kübler, H. Gross, H. Moor, *Ultramicroscopy* **3**, 161 (1978).
21. W. Kühlbrandt, J. Dietrich, W. Haase, unpublished data.
22. M. Cyrklaff, M. Auer, W. Kühlbrandt, G. A. Scarborough, *EMBO J.* **14**, 1854 (1995).
23. K. H. Rhee, G. A. Scarborough, R. Henderson, *EMBO J.* **21**, 3582 (2002).
24. J. P. Hennessey, G. A. Scarborough, *J. Biol. Chem.* **263**, 3123 (1988).


25. We thank W. Haase for performing the freeze-fracture electron microscopy, and D. Stokes and M. Palmgren for discussion. The model coordinates have been deposited in the Protein Data Bank (accession code 1MHS).


**Supporting Online Material**

www.sciencemag.org/cgi/content/full/1072574/DC1
Methods
Figs. S1 to S3
Table S1
References


5 April 2002; accepted 25 July 2002
Published online 8 August 2002;
10.1126/science.1072574
Include this information when citing this paper.


# Nitrogenase MoFe-Protein at 1.16 Å Resolution: A Central Ligand in the FeMo-Cofactor


**Oliver Einsle,[1,2] F. Akif Tezcan,[2] Susana L. A. Andrade,[1,2] Benedikt Schmid,[2] Mika Yoshida,[1,2] James B. Howard,[3] Douglas C. Rees[1,2]***



**A high-resolution crystallographic analysis of the nitrogenase MoFe-protein reveals a previously unrecognized ligand coordinated to six iron atoms in the center of the catalytically essential FeMo-cofactor. The electron density for this ligand is masked in structures with resolutions lower than 1.55 angstroms, owing to Fourier series termination ripples from the surrounding iron and sulfur atoms in the cofactor. The central atom completes an approximate tetrahedral coordination for the six iron atoms, instead of the trigonal coordination proposed on the basis of lower resolution structures. The crystallographic refinement at 1.16 angstrom resolution is consistent with this newly detected component being a light element, most plausibly nitrogen. The presence of a nitrogen atom in the cofactor would have important implications for the mechanism of dinitrogen reduction by nitrogenase.**


Biological nitrogen fixation provides the dominant route for the transformation of atmospheric dinitrogen into a bioavailable form, ammonia (*1–4*). This process is catalyzed by the enzyme nitrogenase, which consists of two component metalloproteins, the Fe-protein and the MoFe-protein. The homodimeric Fe-protein couples adenosine 5′-triphosphate hydrolysis to interprotein electron transfer and is the only known mechanistically competent source of electrons for the catalytically active component, the MoFe-protein. The latter is organized as an $\alpha_2\beta_2$ tetramer that contains two

copies each of two unique polynuclear metal clusters designated the P-cluster and the FeMo-cofactor. Whereas the P-cluster likely participates in interprotein electron transfer, the FeMo-cofactor is the active site of substrate binding and reduction. Despite detailed structural information and a multitude of kinetic, spectroscopic, and theoretical studies, little is known about the mechanistic details of dinitrogen reduction by nitrogenase (*5*), particularly the site and mode of substrate binding.

The structures of the P-cluster and FeMo-cofactor in the MoFe-protein have been determined crystallographically at resolutions between 2.8 and 1.6 Å (*6*–*12*). The FeMo-cofactor, with composition [Mo:7Fe:9S]:homocitrate, is coordinated to the protein through the side chains of only two residues bound to Fe and Mo sites located at opposite ends of the cluster. Perhaps the most unusual feature of the cofactor in these structures is the trigonal prismatic arrangement of the six central iron atoms. These iron atoms lie on the surface of a sphere with a radius of 2.0 Å from the cofactor center and are each coordinated to three inorganic sulfur atoms. Furthermore, all nine sulfur atoms of the FeMo-cofactor are themselves equidistant from the center on a second sphere with a radius of 3.3 Å. The structure of the P-cluster, with composition [8Fe:7S], can be considered composed of two [4Fe:3S] subclusters that are bridged by a hexacoordinate S, with the overall assembly coordinated to the protein through six cysteine ligands.

Analysis of crystallographic structures of the MoFe-protein at resolutions up to 1.7 Å (*13*) indicated a significant (>6σ), positive $F_o - F_c$ difference density peak in the central cavity of the FeMo-cofactor. However, the corresponding $2F_o - F_c$ electron density maps did not show this feature. This contrasting behavior for the two maps suggested that the scattering properties of the whole cofactor might perturb the calculated electron density in its center through the influence of series termination effects. These are a well-known phenomenon in Fourier analyses, and in crystallography lead to resolution-dependent ripples around atomic positions (*14*–*16*); the effect is particularly pronounced around regions of high electron density such as metal sites. To illustrate the effect, the electron-density distribution, ρ(*r*), adjacent to an iron atom can be calculated as a function of the high-resolution limit from the expression (*16*).

$$\rho(r) = \int_0^{1/d_{max}} 4\pi s^2 f_{Fe}(s) \frac{\sin 2\pi sr}{2\pi sr} \, ds \qquad (1)$$

where $f_{Fe}$ is the atomic form factor for iron; $s = 1/d$, where $d$ is the resolution; and $d_{max}$ is the high-resolution limit for integration. If the Fourier transform is truncated by choosing a finite integration limit instead of $1/d_{max} = \infty$, the calculated ρ(*r*) will show resolution-dependent series termination errors (Fig. 1). At a distance of $r = 2.0$ Å from an iron atom, reminiscent of the situation in the central cavity of the FeMo-cofactor, an artificial minimum with negative electron density is created for $d_{max}$ (resolution) between 1.6 and 2.5 Å.

To model the diffraction behavior inside the FeMo-cofactor, the influence of the entire [Mo:7Fe:9S] unit must be considered. When Eq. 1 is used to calculate the scattering contributions from the various individual components, it is apparent that the density in the central cavity is influenced mainly by the six iron atoms at 2.0 Å and the nine sulfur atoms at 3.3 Å (Fig. 2). At lower resolutions, the negative ripples surrounding these multiple iron and sulfur atoms combine to produce sufficiently negative electron density in the cofactor center to completely obscure the electron density of a light atom at this site. Consequently, this implies that the "hole" at the center of the cofactor in the $2F_o - F_c$ electron density map is an artifact, rather than the peak in the $F_o - F_c$ difference density map (*16*).

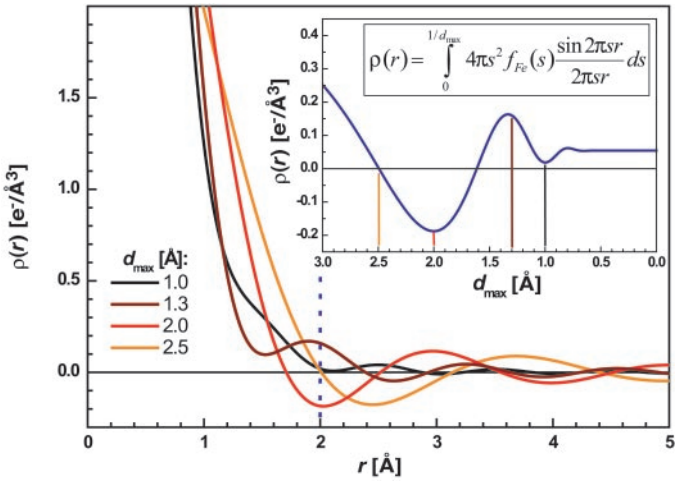


**Fig. 1.** The effect of series termination errors on the resolution-dependent electron density profile around an iron atom. A plot of electron density ρ(*r*) versus distance *r* (Eq. 1) shows varying effects for high-resolution limits $d_{max}$ of 1.0 Å (black), 1.3 Å (brown), 2.0 Å (red), and 2.5 Å (orange). When ρ(*r*) is plotted versus $d_{max}$ for the distance $r = 2.0$ Å (as found in the FeMo-cofactor), a characteristic profile is obtained with resolution-dependent maxima and minima (**inset**).

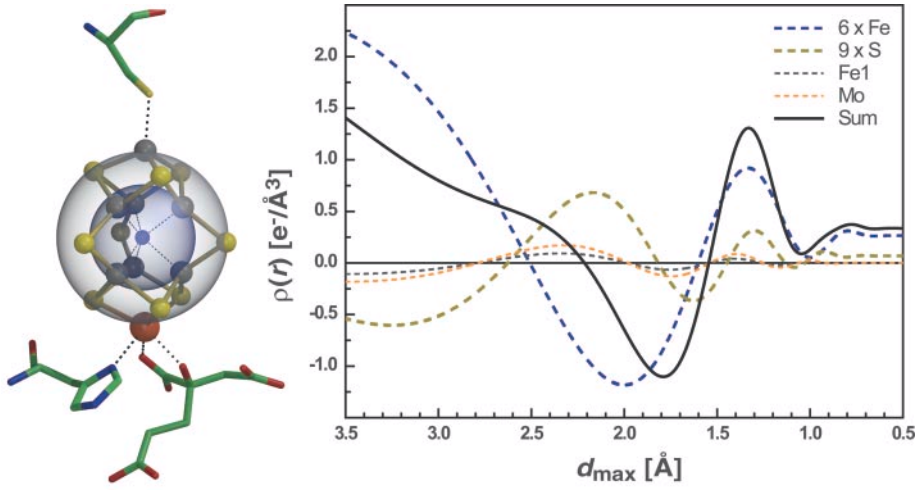


**Fig. 2.** Contributions of individual atom types to the resolution-dependent electron density profile in the central cavity of the FeMo-cofactor. Six iron atoms and all nine of the cluster's sulfur atoms are located on two concentric spheres. Having identical distances from the center (3.3 Å for sulfur, 2.0 Å for iron), they are the main contributors to the electron density profile there. The apical iron and molybdenum atoms exert only a minor influence. Plots of ρ(*r*) versus $d_{max}$, calculated analogously to Fig. 1 (inset), illustrate this effect. The curves for six iron atoms at 2.0 Å (blue), nine sulfur atoms at 3.3 Å (dark yellow), and one apical iron (Fe1, gray) and the molybdenum (orange) at 3.5 Å are shown. The sum of of all these contributions is shown in black.

[1]Howard Hughes Medical Institute, [2]Division of Chemistry and Chemical Engineering, California Institute of Technology, Mail Code 147-75CH, Pasadena, CA 91125, USA. [3]Department of Biochemistry, University of Minnesota, Minneapolis, MN 55455, USA.

*To whom correspondence should be addressed. E-mail: dcrees@caltech.edu

As indicated in Fig. 2, series termination effects become less pronounced with increasing resolution. Hence we initiated the structure determination of the *Azotobacter vinelandii* MoFe-protein at a sufficiently high resolution to overcome their influence (*17*). To achieve this, we improved the quality of dithionite-reduced MoFe-protein crystals to permit data collection and refinement of the structure (Table 1) at 1.16 Å resolution to $R = 0.123$, with a diffraction component precision index [DPI (*18*)], a measure of the coordinate error, of 0.027 Å. These crystals contain two $\alpha_2\beta_2$ tetramers per asymmetric unit, and consequently four crystallographically independent copies of the FeMo-cofactor are present. Each copy clearly shows electron density at the center of the FeMo-cofactor in maps calculated with both $F_o - F_c$ and $2F_o - F_c$ Fourier coefficients (Fig. 3).

To characterize the atomic identity of the ligand at the center of the cofactor, we calculated a resolution-dependent electron density profile, analogous to that of Fig. 2, from the experimental diffraction data, which confirms the substantial impact of series termination errors (Fig. 4). The absolute values of electron density differ from those of the theoretical model (Fig. 2), owing to the absence of some low-resolution reflections, including the $F(000)$ term, in the experimental data. Consequently, the experimental electron-density minimum is even more pronounced than in the theoretical model. The electron density at the cofactor center, as determined from the observed structure factor amplitudes and phases calculated from a model lacking a central atom (black dots), is negative for all resolutions <1.55 Å. If, however, a purely theoretical curve is generated with both calculated structure factor amplitudes and phases from this same model (black line), the density at the cofactor center is substantially lower. Clearly, a central atom needs to be added to the model to reproduce the experimentally observed data. If the same model calculations are performed with an atom in the center of the cavity, the results are qualitatively similar and demonstrate that the destructive interference of the surrounding atoms is sufficient to obliterate the densities of a carbon, a nitrogen, or an oxygen atom at this position, although not that of a sulfur atom.

Unambiguous identification of an atom type solely from its electron density is problematic, even at atomic resolution. We considered carbon, nitrogen, oxygen, and sulfur as chemically plausible candidates

**Table 1.** Data collection and refinement statistics. For the calculation of $R_{free}$, 1% of the observed reflections were removed at random before refinement. a.u., asymmetric unit; ref., refinement; FOM, figure of merit; rmsd, root mean square deviation.

| | |
|---|---|
| Resolution range | 50.0–1.16 Å |
| Space group | $P2_1$ |
| Unit cell | $a$ = 108.3 Å<br>$b$ = 131.6 Å<br>$c$ = 159.2 Å<br>β = 108.3° |
| $\alpha_2\beta_2$ per a.u. | 2 |
| Total reflections before adding partials | 25,851,165 |
| Independent reflections | 1,390,520 |
| Overall data redundancy | 2.5 |
| Completeness (outer shell) | 95.6% (90.0%) |
| $R_{merge}$* (outer shell) | 0.090 (0.485) |
| $I/\sigma(I)$ (outer shell) | 10.0 (1.6) |
| Atoms in ref. (non-H) | 37,388 |
| Protein residues | 3,708 |
| Water molecules | 5,025 |
| Mean $B$ value | 15.6 Å$^2$ |
| Overall FOM | 0.923 |
| $R$-factor ($R_{free}$)† | 0.123 (0.149) |
| rmsd bond lengths | 0.020 Å |
| rmsd bond angles | 2.251° |
| Estimated coordinate error (DPI)‡ | 0.027 Å |

*$R_{merge} = \Sigma_{hkl}|\langle I\rangle - I|/\Sigma_{hkl}|I|$. †$R = \Sigma_{hkl}||F_{obs}| - |F_{calc}||/\Sigma_{hkl}|F_{obs}|$. ‡The diffraction component precision index (DPI) was calculated according to Cruickshank (*18*).

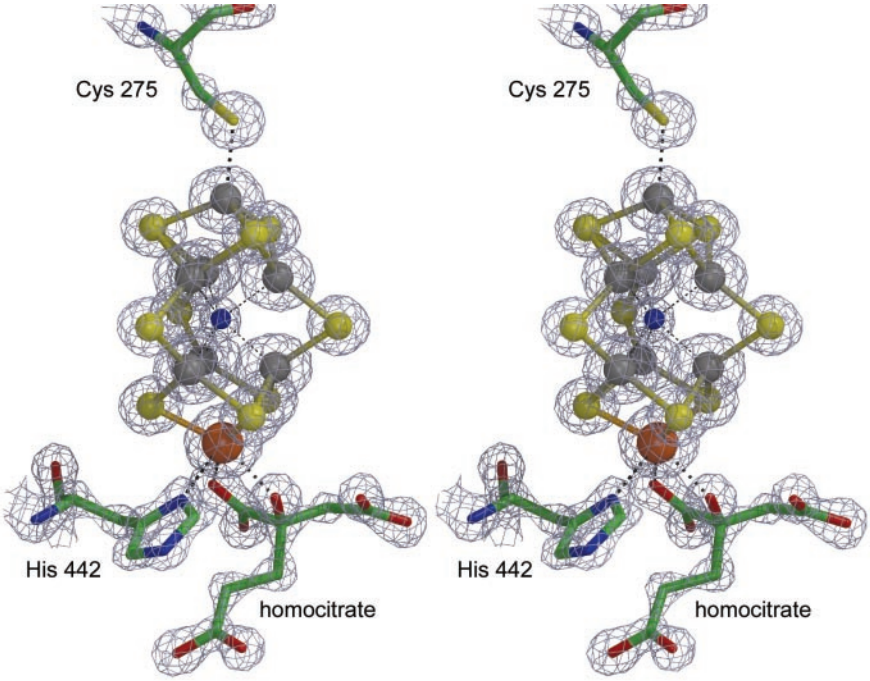


**Fig. 3.** Stereo representation of the FeMo-cofactor with the central ligand modeled as a nitrogen atom. The electron density map shown is a weighted $2F_o - F_c$ map of the 1.16 Å resolution structure of dithionite-reduced *A. vinelandii* MoFe-protein contoured at 3σ.

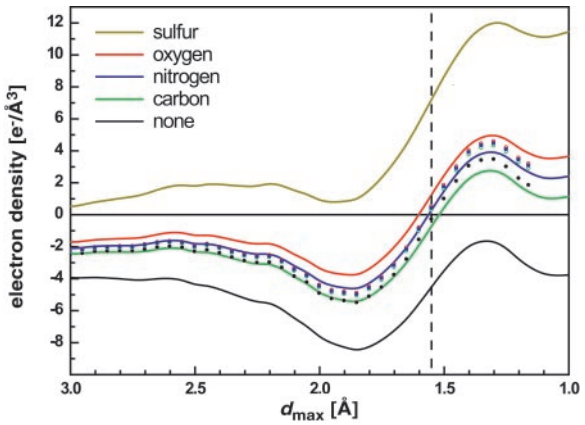


**Fig. 4.** Resolution-dependent electron density profiles as derived from the complete 1.16 Å resolution structure of dithionite-reduced *A. vinelandii* MoFe-protein. Solid lines are pure $F_{calc}$ electron density values, whereas dotted curves are read from actual $F_{obs}\cdot\varphi_{calc}$ maps computed with the experimental structure factor amplitudes. The calculated density without a central ligand in the cofactor (black line) is well below the one observed in the experimental map (black dots). The latter further shows that positive density at the central position is obtained only at resolutions beyond 1.55 Å. A sulfur atom in the central cavity, however, gives a profile (dark yellow line) that at no resolution leads to negative electron density. Thus, a sulfur atom in the structure would not have been missed. If carbon (green line), nitrogen (blue line), or oxygen (red line) is placed in the center, their density still disappears, but experimental densities from structures refined with any of these atoms result in nearly identical curves (green, blue, and red dots), which agree most closely to the theoretical curve with nitrogen.

for the central atom and tested each with the available diffraction data. Because the surrounding atoms of the FeMo-cofactor are well defined and show very low temperature factor anisotropy, we assumed that the central ligand is fully occupied; partial occupancy should create at least a slight positional displacement in its environment. Although the possibility of a central sulfur atom was considered in initial models of the cofactor, of these four elements, we consider sulfur as the least likely candidate for the central atom because the observed density would allow only partial occupancy, the distances to the surrounding iron atoms are too short, and the destructive interference of the surrounding atoms is not sufficient to entirely cancel the density of the sulfur in the lower resolution structures, contrary to what is observed (Fig. 4). Refinement of a carbon, nitrogen, or oxygen atom at the central position in all cases yielded temperature factors for this site (C: 12.6 ± 2.2 Å$^2$; N: 14.0 ± 2.0 Å$^2$; O: 14.8 ± 2.5 Å$^2$) that correspond well to the values observed for the surrounding irons (12.2 ± 1.1 Å$^2$). Although the density for the ligand tends to be more anisotropic than for the inorganic components of the cofactor, it is not compatible with an ordered diatomic or larger species. Consequently, although the identity of the central ligand in the FeMo-cofactor cannot be unambiguously established from the crystallographic analysis, from the properties of the resolution-dependent electron-density profile (Fig. 4), and from the interaction of nitrogenase with dinitrogen and ammonia, we have tentatively assigned this central ligand as a fully occupied N.

Interatomic distances in the FeMo-cofactor between metals and the central nitrogen are summarized in Fig. 5. The central nitrogen ligand is hexacoordinate, with average iron-nitrogen distances of 2.00 ± 0.05 Å. This overall arrangement resembles that of a previously characterized cobalt carbonyl cluster containing interstitial nitrogen surrounded by a trigonal prismatic arrangement of metal (*19*), with an average Co-N distance of 1.94 Å. With average N–Fe–S bond angles of 102° ± 2°, the central ligand completes an approximately tetrahedral coordination environment for the six irons surrounding this group; consequently, it is no longer true that these iron sites are "three-coordinate" (*6*), at least in the dithionite-reduced form of the MoFe-protein.

The presence of a ligand in the center of the FeMo-cofactor, particularly a nitrogen, has important implications for understanding the properties of nitrogenase. One potentially relevant observation is the evidence from electron spin echo envelope modulation (ESEEM) studies for one or more nitrogen nuclei interacting with the FeMo-cofactor (*20–22*). Whereas the ESEEM signals have been assigned to nitrogen atoms of surrounding protein residues, the presence of a nitrogen atom in the cofactor suggests an alternate, nonprotein, source for at least some of the signal. Although a central nitrogen atom could be a structural component of the cofactor, it is difficult to conceive of a process whereby it is inserted without some relation to dinitrogen reduction. Indeed, a monoatomic nitrogen is consistent with the Thorneley and Lowe (*23*) kinetic model that requires the resting state of the MoFe-protein to be reduced by three electrons before dinitrogen can bind. This may reflect the need to replenish the electrons used in reducing the nitrogen to the level of nitride ($N^{3-}$) before it can be liberated as ammonia.

Theoretical studies of substrate binding to the FeMo-cofactor have indicated that the center of the trigonal prismatic arrangement of irons provides favorable interaction sites for dinitrogen and its reduction products (*24–26*). Furthermore, the spacing of iron atoms around this central site in the FeMo-cofactor closely parallels that of the iron surfaces used as catalysts for dinitrogen reduction in the industrial Haber-Bosch process (*27*). However, the distances between irons in the cofactor are longer (2.63 Å) than in regular metallic iron (2.47 Å), and such strained metal surfaces have been modeled to be particularly reactive as catalysts for dinitrogen dissociation (*28*). Notwithstanding the enormous disparity of reaction conditions, the parallels between the arrangement of metals in the nitrogenase FeMo-cofactor and the catalyst for the Haber-Bosch process suggest the possibility of common mechanistic elements in the reduction of dinitrogen to ammonia.

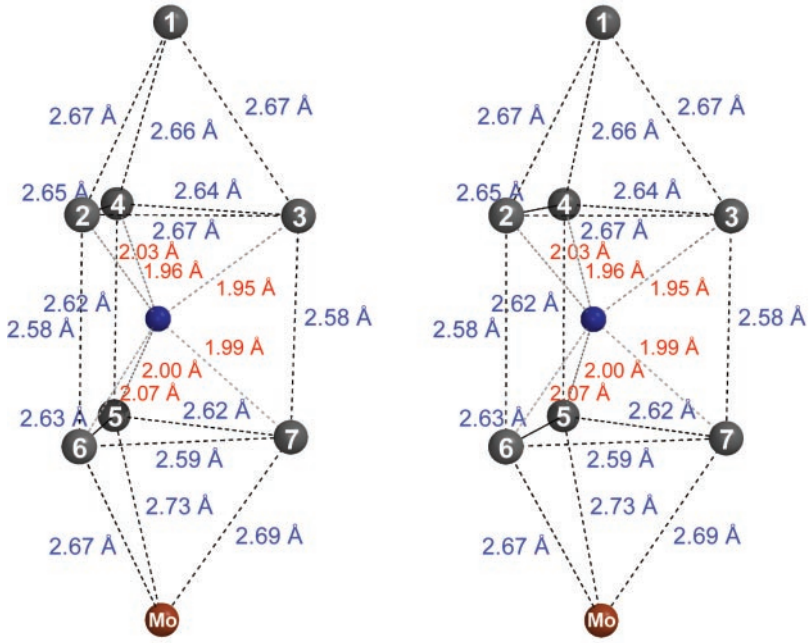


**Fig. 5.** Stereo representation of interatomic distances in the FeMo-cofactor. Mean values for the individual distances are the averages of the four crystallographically independent copies of the cofactor in the structure of the dithionite-reduced *A. vinelandii* MoFe-protein. Standard deviations are 0.01 Å for metal-metal and 0.03 Å for metal-nitrogen distances.

## References and Notes


1. B. K. Burgess, D. J. Lowe, *Chem. Rev.* **96**, 2983 (1996).
2. J. B. Howard, D. C. Rees, *Chem. Rev.* **96**, 2965 (1996).
3. B. E. Smith, *Adv. Inorg. Chem.* **47**, 159 (1999).
4. J. Christiansen, D. R. Dean, L. C. Seefeldt, *Annu. Rev. Plant Physiol. Plant Mol. Biol.* **52**, 269 (2001).
5. D. C. Rees, J. B. Howard, *Curr. Opin. Chem. Biol.* **4**, 559 (2000).
6. J. Kim, D. C. Rees, *Science* **257**, 1677 (1992).
7. _____, *Nature* **360**, 553 (1992).
8. M. K. Chan, J. Kim, D. C. Rees, *Science* **260**, 792 (1993).
9. J. Kim, D. Woo, D. C. Rees, *Biochemistry* **32**, 7104 (1993).
10. J. T. Bolin, N. Campobasso, S. W. Muchmore, T. V. Morgan, L. E. Mortenson, in *Molybdenum Enzymes, Cofactors and Model Systems*, E. I. Stiefel, D. Coucouvanis, W. E. Newton, Eds. (ACS Symposium Series 535, American Chemical Society, Washington, DC, 1993), pp. 186–195.
11. J. W. Peters *et al.*, *Biochemistry* **36**, 1181 (1997).
12. S. M. Mayer, D. M. Lawson, C. A. Gormal, S. M. Roe, B. E. Smith, *J. Mol. Biol.* **292**, 871 (1999).
13. O. Einsle *et al.*, unpublished data.
14. W. L. Bragg, J. West, *Philos. Mag.* **10**, 823 (1930).
15. R. W. James, *Acta Crystallogr.* **1**, 132 (1948).
16. W. Cochran, H. Lipson, in *The Determination of Crystal Structures*, W. L. Bragg, Ed. (Cornell Univ. Press, Ithaca, NY, ed. 3, 1966).
17. Materials and methods are available as supporting material on *Science* Online.
18. D. W. J. Cruickshank, *Acta Crystallogr.* **D55**, 583 (1999).
19. S. Martinengo, G. Ciani, A. Sironi, B. T. Heaton, J. Mason, *J. Am. Chem. Soc.* **101**, 7095 (1979).

20. H. Thomann *et al.*, *J. Am. Chem. Soc.* **109**, 7913 (1987).
21. A. E. True, P. McLean, M. J. Nelson, W. H. Orme-Johnson, B. M. Hoffman, *J. Am. Chem. Soc.* **112**, 651 (1990).
22. H. I. Lee, K. S. Thrasher, D. R. Dean, W. E. Newton, B. M. Hoffman, *Biochemistry* **37**, 13370 (1998).
23. R. N. F. Thorneley, D. J. Lowe, in *Molybdenum Enzymes*, T. G. Spiro, Ed. (Wiley-Interscience, New York, 1985), vol. 1, pp. 221–230.
24. H. B. Deng, R. Hoffmann, *Angew. Chem. Int. Ed. Engl.* **32**, 1062 (1993).
25. K. K. Stavrev, M. C. Zerner, *Chem. Eur. J.* **2**, 83 (1996).
26. P. E. M. Siegbahn, J. Westerberg, M. Svensson, R. H. Crabtree, *J. Phys. Chem. B* **102**, 1615 (1998).
27. G. Ertl, H. Knözinger, J. Weitkamp, Eds., *Handbook of Heterogeneous Catalysis* (VCH, New York, 1997), vol. 4.
28. A. Logadottir, J. K. Nørskov, *Surf. Sci.* **489**, 135 (2001).
29. This work was supported by NIH. Stanford Synchrotron Radiation Laboratory operations are funded by the U.S. Department of Energy (DOE), Office of Basic Energy Sciences, and NIH. F.A.T. acknowledges the Burroughs Wellcome Fund and the Helen Hay Whitney Foundation for postdoctoral fellowships. We thank J. C. Peters, J. E. Bercaw, and H. B. Gray for enlightening discussions. Coordinates of the refined MoFe-protein structure have been deposited in the Protein Data Bank (accession code 1M1N).

**Supporting Online Material**
www.sciencemag.org/cgi/content/full/297/5587/1696/DC1
Materials and Methods
References

13 May 2002; accepted 26 June 2002

# Cooperation of GGAs and AP-1 in Packaging MPRs at the Trans-Golgi Network

**Balraj Doray,[1]*† Pradipta Ghosh,[1]* Janice Griffith,[2] Hans J. Geuze,[2] Stuart Kornfeld[1]‡**

**The Golgi-localized, γ-ear–containing, adenosine diphosphate ribosylation factor–binding proteins (GGAs) are multidomain proteins that bind mannose 6-phosphate receptors (MPRs) in the Golgi and have an essential role in lysosomal enzyme sorting. Here the GGAs and the coat protein adaptor protein–1 (AP-1) were shown to colocalize in clathrin-coated buds of the trans-Golgi networks of mouse L cells and human HeLa cells. Binding studies revealed a direct interaction between the hinge domains of the GGAs and the γ-ear domain of AP-1. Further, AP-1 contained bound casein kinase–2 that phosphorylated GGA1 and GGA3, thereby causing autoinhibition. This could induce the directed transfer of the MPRs from GGAs to AP-1. MPRs that are defective in binding to GGAs are poorly incorporated into AP-1–containing clathrin-coated vesicles. Thus, the GGAs and AP-1 interact to package MPRs into AP-1–containing coated vesicles.**

In higher eukaryotic cells, the sorting of newly synthesized acid hydrolases to lysosomes is dependent on the mannose 6-phosphate (Man-6-P) recognition system (*1*). A key step in this pathway is the binding of the Man-6-P–tagged hydrolases to MPRs in the trans-Golgi network (TGN). The receptors are then packaged into transport vesicles for delivery to endosomal compartments, where the hydrolases are released and transferred to lysosomes. The MPRs are localized to AP-1–containing clathrin-coated vesicles (AP-1–CCVs) at the TGN, implicating AP-1 as the coat protein involved in transport vesicle assembly (*2*). The MPRs also bind to the GGA family (*3*–*5*). The GGAs are modular proteins with four domains: an $NH_2$-terminal VPS-27, Hrs, and STAM (VHS) domain, then a GGA and TOM (GAT) domain, a connecting hinge segment, and a COOH-terminal γ-adaptin ear (GAE) domain. The GAT domain binds adenosine diphosphate ribosylation factor–guanosine 5′-triphosphate complexes and mediates recruitment of the protein from the cytosol onto the TGN (*6*, *7*). The VHS domain then interacts specifically with the acidic cluster–dileucine (AC-LL) motif in the cytoplasmic tails of the MPRs (*3*–*5*, *8*, *9*). Mutations in the AC-LL motif impair acid hydrolase sorting and decrease binding of the MPRs to the GGAs but not to AP-1, indicating that the GGAs have a major role in the sorting process (*4*, *10*, *11*). One explanation for these findings is that the GGAs and AP-1 function in parallel to package MPRs into different vesicular carriers at the TGN, as has been proposed to occur in yeast (*12*). Alternatively, the GGAs could bind the MPRs and facilitate their entry into forming AP-1–CCVs. We sought to distinguish between these two possibilities.

We first examined the distribution of GGA2 and AP-1 in mouse L cells by means of the cryo-immunogold technique. If the two proteins nucleate their own transport vesicles in the TGN, then they should be detected on separate coated buds and vesicles in the TGN, whereas if they cooperate in the packaging of MPRs, they might be found together. GGA2 was associated with tubules, buds, and CCVs at the TGN (Fig. 1A). In double-labeling experiments, GGA2 and AP-1 colocalized on the buds and CCVs (Fig. 1, B to D; Tables 1 and 2). About 50% of GGA2 was found on clathrin-coated TGN membranes, of which half was on identifiable buds. Forty-one percent of the coated TGN buds contained both proteins (Table 2). Similarly, GGA1 and AP-1 colocalized in coated buds at the TGN of HeLa cells. These findings are consistent with an interaction between the two proteins.

To examine this possibility, we expressed the three GGAs in SF9 insect cells and tested them for binding to glutathione *S*-transferase (GST) fusion proteins containing either the γ-ear domain or the hinge segment of AP-1 coupled to glutathione beads in pulldown experiments. All three GGAs bound to the GST–γ ear fusion protein, whereas no binding to the GST-γ hinge was detected (Fig. 2A). The binding was direct because purified GGAs also bound to the GST-γ ear (Fig. 2B). The GGAs interacted poorly with the ear domains of AP-2 and GGA2, showing that the binding was specific for the AP-1–γ ear (Fig. 2C). Binding was lost when the GGA1 hinge was truncated from 429 to 370 residues (Fig. 2D). Thus, the hinge segments of the GGAs bind to the γ-ear domain of AP-1. That truncated GGA1 lacking the hinge traps the MPRs in the TGN (*3*) supports the idea that the GGA–AP-1 interaction is essential for normal MPR trafficking.

The fact that the GGAs interact with AP-1 but are undetectable in isolated CCVs (*13*) raises the possibility that they bind the MPRs in the TGN and present them to AP-1 for packaging into CCVs. In this case there should be a mechanism whereby the GGAs release their cargo molecules upon interacting with AP-1. MPR binding to the VHS domains of GGA1 and GGA3 is regulated by competitive binding of an AC-LL motif in the hinge segment (*14*). This intramolecular binding requires casein kinase–2 (CK-2)–mediated phosphorylation of a serine located three residues upstream of the acidic cluster. Meresse *et al.* have reported that AP-1 isolated from CCVs has an associated CK-2–type activity (*15*). If this kinase were to

[1]Department of Internal Medicine, Washington University School of Medicine, 660 South Euclid Avenue, St. Louis, MO 63110, USA. [2]Department of Cell Biology, University Medical Center and Institute for Biomembranes, Utrecht University, 3584 CX Utrecht, Netherlands.

*These authors contributed equally to this work.
†Present address: Genome Institute of Singapore, 1 Science Park Road, The Capricorn #05-01 Singapore 117528.
‡To whom correspondence should be addressed. E-mail: skornfel@im.wustl.edu